inorganics

MDPI

Article

Hydrothermal Treatment of Tannin: A Route to Porous Metal Oxides and Metal/Carbon Hybrid Materials

Flavia L. Braghiroli [1], Vanessa Fierro [1], Andrzej Szczurek [1], Philippe Gadonneix [1], Jaafar Ghanbaja [2], Julien Parmentier [3], Ghouti Medjahdi [4] and Alain Celzard [1,*]

1 Institut Jean Lamour, UMR CNRS—Université de Lorraine n° 7198, ENSTIB, 27 rue Philippe Séguin, CS 60036, 88026 Epinal CEDEX, France; flavialegab@yahoo.com (F.L.B.); vanessa.fierro@univ-lorraine.fr (V.F.); jahman19@wp.eu (A.S.); philippe.gadonneix@univ-lorraine.fr (P.G.)

2 Institut Jean Lamour, UMR CNRS—Université de Lorraine n° 7198, ENSTIB, Parc de Saurupt, CS 50840, F-54011 Nancy CEDEX, France; jaafar.ghanbaja@univ-lorraine.fr

3 Institut de Science des Matériaux de Mulhouse, LRC CNRS 7228, Université de Haute Alsace, 15 rue Jean Starcky, 68057 Mulhouse, France; julien.parmentier@uha.fr

4 Institut Jean Lamour, UMR CNRS—Université de Lorraine n° 7198, Faculté des Sciences, Bd des Aiguillettes, BP 239, 54506 Vandoeuvre-lès-Nancy CEDEX, France; Ghouti.Medjahdi@univ-lorraine.fr

* Correspondence: alain.celzard@univ-lorraine.fr; Tel.: +33-329-29-61-14; Fax: +33-329-29-61-38

Academic Editor: Samuel Bernard
Received: 21 December 2016; Accepted: 20 January 2017; Published: 24 January 2017

Abstract: In the present paper, porous materials were prepared from the hydrothermal treatment of aqueous solutions of tannin, a renewable phenolic resource extracted from tree barks, containing dissolved salts of transition metals: V, Cr, Ni and Fe. Hydrothermal treatment produced carbonaceous particles doped with the aforementioned metals, and such materials were treated according to two different routes: (i) calcination in air in order to burn the carbon and to recover porous oxides; (ii) pyrolysis in inert atmosphere so as to recover porous metal/carbon hybrid materials. The nature of the metal salt was found to have a dramatic impact on the structure of the materials recovered by the first route, leading either to nano-powders (V, Cr) or to hollow microspheres (Ni, Fe). The second route was only investigated with iron, leading to magnetic Fe-loaded micro/mesoporous carbons whose texture, pore volumes and surface areas gradually changed with the iron content.

Keywords: hydrothermal treatment; tannin; metal oxide nanoparticles; hollow microspheres; iron/carbon hybrid materials

1. Introduction

Over the past decades, magnetic materials with various shapes, sizes and crystal structures have been applied in different fields, i.e., for data information storage, photonics and electronics [1–3], magnetic sensors [4,5], catalysis [6], environmental remediation [7,8] as well as in biomedicine, drug delivery, magnetic resonance imaging and pharmaceutical areas [9–11]. Metal nanostructures were shown to present enhanced electronic, magnetic, optical and chemical properties compared to those of already existing bulk materials. However, the use of pure metal magnetic nanoparticles such as iron (Fe) is not always possible due to its instability in air. It can indeed ignite spontaneously at room temperature [12], be dissolved in acidic and basic media, and can easily agglomerate. These problems may drastically limit the application of metal nanostructures [13,14]. To cope with such limitations, the deposition of a protective shell was suggested for improving the chemical stability of metal nanoparticles. Compared to other shells used for that purpose made of, e.g., metal oxides [15], silica [12,16], titanium [17] or polymers [18,19], carbon materials are attractive for the encapsulation

process because they combine two main advantages: (i) high chemical and physical stability [20], and (ii) good biocompatibility and high surface activity [21].

Metal elements are also able to form a broad range of oxide compounds, and such materials may present many structures exhibiting metallic, semiconductor or insulator character, thereby allowing their use in most technological fields such as in electronic and energy storage devices, fuel cells and especially catalysis [22]. Regarding their preparation, the most common methods include co-precipitation [23,24], sonochemical synthesis [25,26], sol–gel [27,28] and hydrothermal synthesis [29–31]. Among the aforementioned methods, hydrothermal carbonisation (HTC) sounds particularly attractive due to several benefits: (i) it is environment-friendly as the reactions take place in aqueous medium in mild conditions of temperature and pressure; (ii) it is cost- and energy-efficient and therefore suitable for industrial processes; (iii) it can lead to many different kinds of materials, e.g., having nanometre size and/or different morphologies, depending on the reaction conditions [32–34].

Metal ions can speed up the HTC process of carbohydrates during the synthesis of carbonaceous materials. Carbohydrate precursors derived from biomass have then been widely applied for the production of metal nanoparticles in a sustainable and environment-friendly manner [35–38]. The present authors also extensively worked on the conversion of bioresources into carbons through HTC. Especially, Mimosa tannin as a natural polyphenol was successfully converted this way into (i) high-surface area carbons made from tannin solution at low pH [39], (ii) N-doped carbon materials [40,41]; (iii) carbon gels without the use of any kind of crosslinker agents [42], and even (iv) microspheres having silver metal particles encapsulated into them [39]. In fact, tannin has excellent antioxidant properties, better than those of phenolic compounds of low molecular weight [43–45]. Antioxidant properties of tannins are related to their free radical scavenging activity but also to their ability to chelate transition metal ions, especially Fe^{2+} and Cu^{2+} [43,46,47].

Therefore, in the present work, Mimosa tannin extracted from the barks of wattle trees was used as a precursor for producing transition metal-based materials through HTC followed by heat treatment in air or under nitrogen flow, thereby leading to various porous materials.

2. Results and Discussion

2.1. Metal Nano/Micro-Oxides

Materials obtained after HTC of various metal salts in the presence of Mimosa tannin, as well as after calcination in air, are presented in Figures 1–4. Depending on the particle sizes, TEM or SEM pictures are presented, which led to the following, important conclusions.

(i) Depending on the nature of the metal salt, different particle morphologies and sizes can be observed after HTC. In the conditions detailed above, vanadium led to the smallest carbonaceous particles (<0.5 μm), themselves appearing to be aggregates of even smaller grains (<20 nm) as seen in Figure 1. Chromium led to very similar materials, as seen in Figure 2, just presenting slightly bigger aggregates (~1 μm). All these metal-doped materials after HTC presented small, poorly spherical carbonaceous particles aggregated together in a nodular, gel-like structure. In contrast, nickel and iron produced bigger (~5 μm) and much more spherical particles showing an apparently solid structure, see Figures 3 and 4, respectively.

(ii) As a result, the materials after calcination in air were also quite different. Those produced from V and Cr were nanocrystals of typical size close to 50 nm in the smallest direction. On the contrary, those derived from Ni and Fe were spherical oxide particles having maintained the rounded shape of their carbonaceous precursors, but with a smaller diameter due to pyrolysis-induced shrinkage.

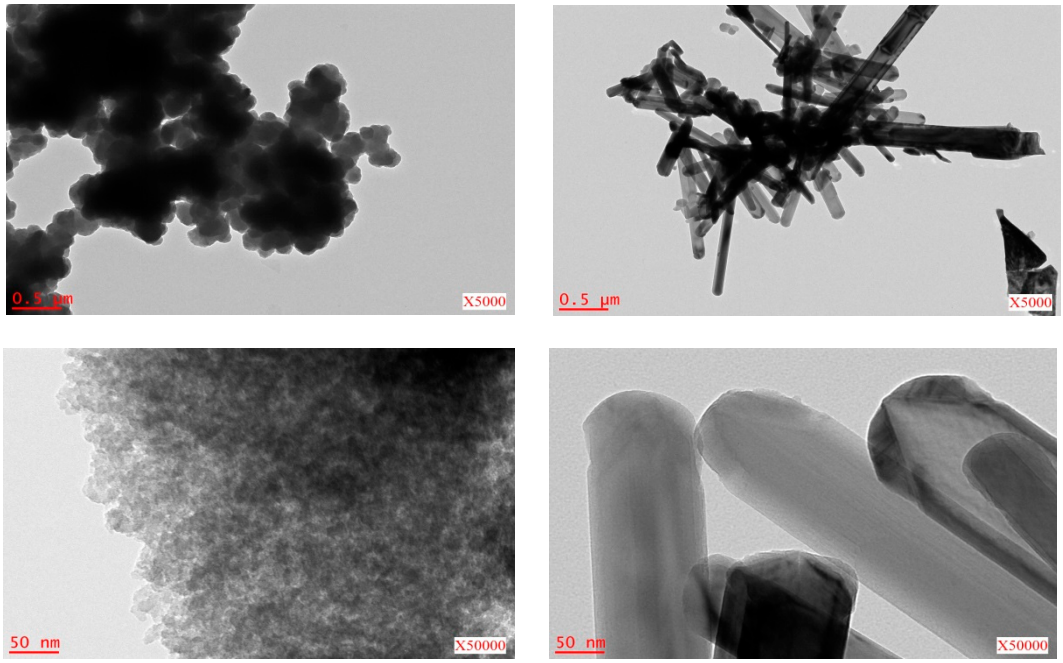

Figure 1. Materials produced by hydrothermal carbonisation (HTC) of $VOSO_4 \cdot 5H_2O$–Mimosa tannin solution at different magnifications: before (**left**) and after (**right**) calcination in air; TEM pictures.

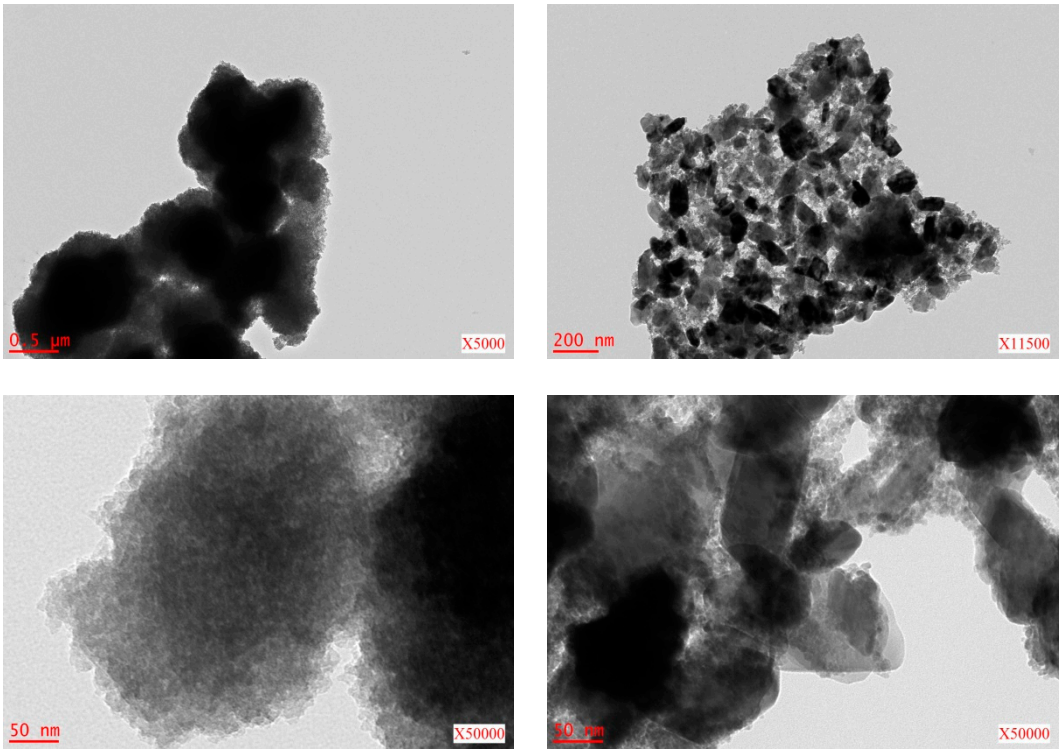

Figure 2. Materials produced by HTC of $(NH_4)_2Cr_2O_7$–Mimosa tannin solution at different magnifications: before (**left**) and after (**right**) calcination in air; TEM pictures.

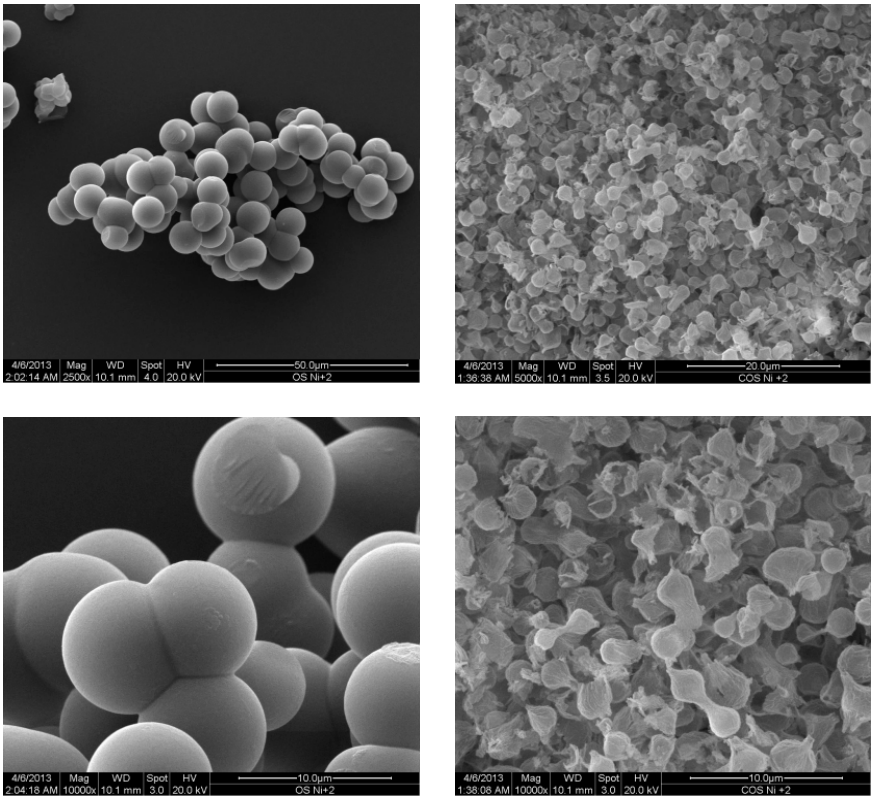

Figure 3. Materials produced by HTC of $Ni(NH_4)_2(SO_4)_2 \cdot 6H_2O$–Mimosa tannin solution at different magnifications: before (**left**) and after (**right**) calcination in air; SEM pictures.

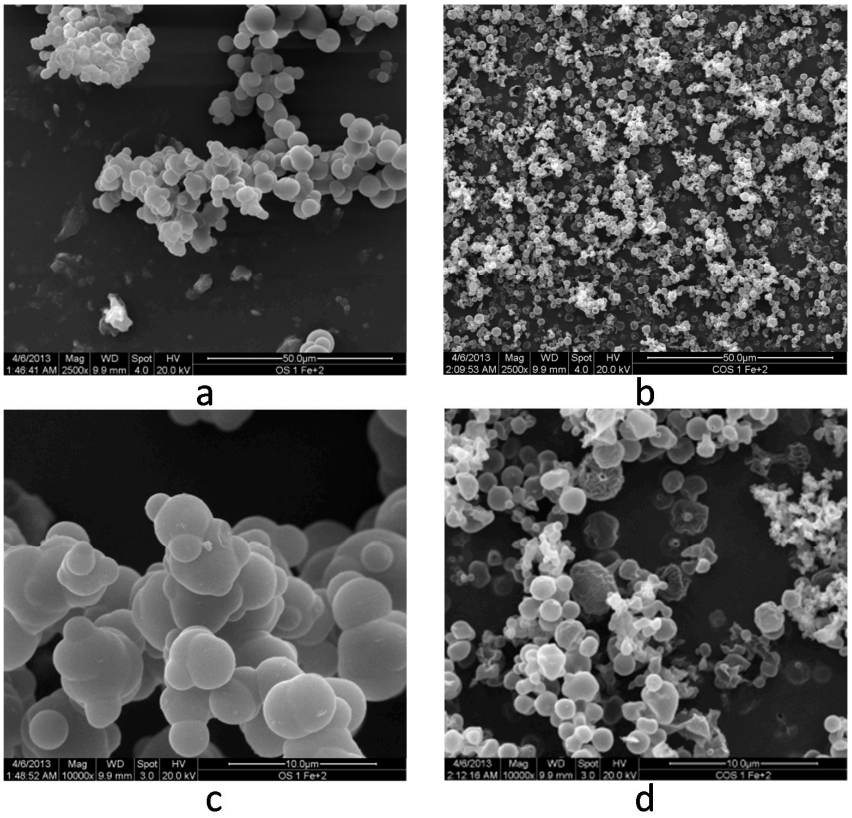

Figure 4. *Cont.*

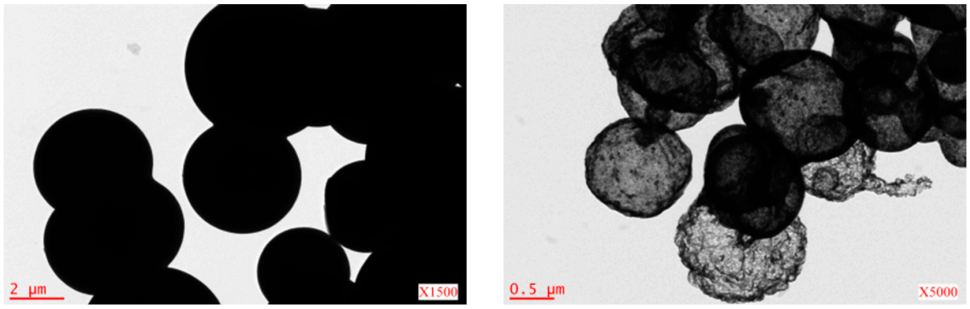

Figure 4. Materials produced by HTC of $(NH_4)_2Fe(SO_4)_2 \cdot 6H_2O$–Mimosa tannin solution at different magnifications: before (**a**,**c**,**e**) and after (**b**,**d**,**f**) calcination in air; SEM (**a**–**d**) and TEM (**e**,**f**) pictures.

Such extreme differences in the behaviour of V and Cr on the one hand, and of Ni and Fe on the other hand, should be explained by the way the corresponding ions bind to tannin during the hydrothermal process. It is indeed well known that tannins dissolved in water are good metal chelators, and this property has been used for centuries for preparing dyes and inks. Considering that nano-oxides were obtained with V and Cr, it can be conjectured that the corresponding ions were chelated everywhere in the tannin-based polymer network. As a result, the metals were highly dispersed in the carbonaceous structure after HTC, leading to extremely small grains after calcination during which recrystallization could occur, as shown by the needles observed in the right part of Figure 1. The corresponding reaction scheme is given in Figure 5, in which a typical oligomer structure is shown (more details can be found elsewhere, e.g., in [48,49] and refs. therein).

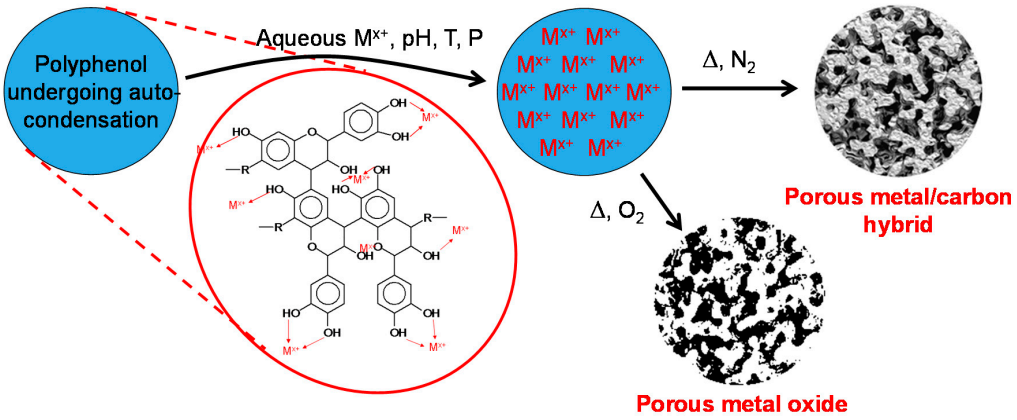

Figure 5. Probable reaction scheme leading to either porous metal/carbon hybrid materials or to metal oxide nano/microparticles after HTC of tannin-metal salt solutions followed by heat-treatment in inert atmosphere or in air, respectively. This scheme applied to V and Cr salts, not to Ni and Fe salts.

The case of Ni and Fe is different. Figures 3 and 4 indeed clearly show that the materials directly obtained after HTC present the typical solid spherical particles known for pure Mimosa tannin treated in hot pressurised water at 180 °C for 24 h [50], whereas such classical morphological features were lost by using V and Cr salts (see again Figures 1 and 2). Homogeneous hollow spherical particles of diameter around 1 µm were thus recovered after calcination in air at 550 °C. At the beginning of the synthesis, a black solution was obtained immediately after mixing tannin with either ammonium nickel sulphate or ammonium iron(II) sulphate, which was converted into a dark suspension in a reddish solution. However, unlike the former chelation mechanism for which metals were homogeneously dispersed in the bulk of the tannin-based crosslinked network and whose polymerisation was forced by the HTC conditions, it is more likely that both Ni and Fe ions were adsorbed from the solution

by the moieties at the surface of carbonaceous tannin microspheres that formed in the autoclave. The scheme presented in Figure 5 is therefore no longer expected to hold in the bulk of the materials but only at their extreme surface. As a consequence, the metal is concentrated in the outer part of the microspheres, leading to the formation of hollow oxide spheres after the carbon was burnt in air.

This mechanism is further supported by the dumbbell-like structure presented by most hollow oxide capsules. Carbonaceous microspheres were indeed not individualised when recovered from the autoclave, but instead were stuck to each other through broad necks. Such a structure is very well seen in the left part of Figures 3 and 4, showing the materials after HTC, as well as the several double-hollow oxide spheres that can be seen in the right part of Figures 3 and 4. TEM pictures of iron and nickel oxide particles are given in Figures 6 and 7 at different magnifications, showing how they are bonded to each other and how thin is their shell. It can also be seen that, for many of them, double-shelled hollow spheres were obtained. However, the mechanism behind the formation of such structures is still unclear. It suggests the chelation of the metal in two steps at the surface of carbonaceous particles growing from the liquid medium submitted to HTC: the smallest one may correspond to the metallic shell condensed on the tannin-based nuclei whereas the biggest one corresponds to the shell that condensed after the particles finished growing.

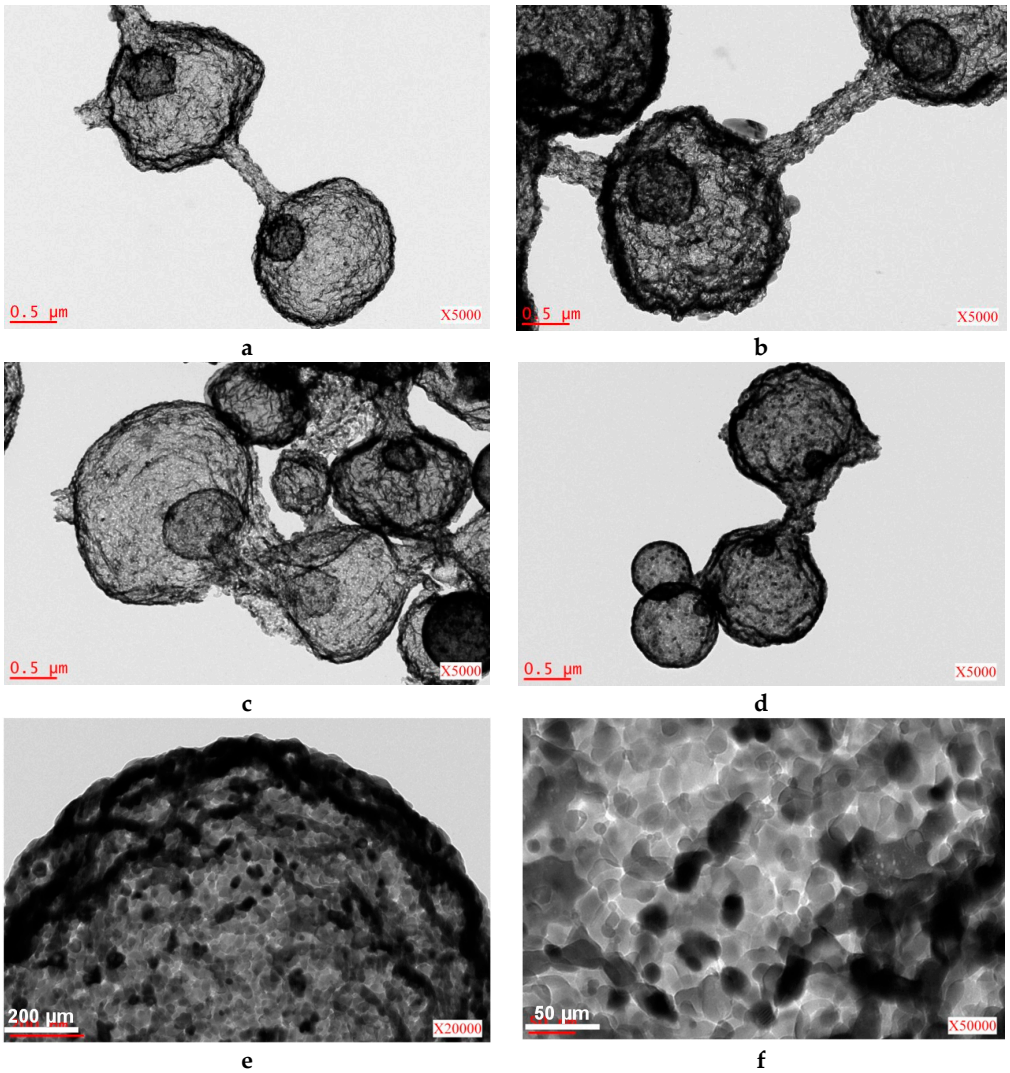

Figure 6. TEM pictures of hollow iron oxide microspheres: (**a**–**d**) general views at the same magnification; (**e**–**f**) same as (**d**) but at higher magnifications.

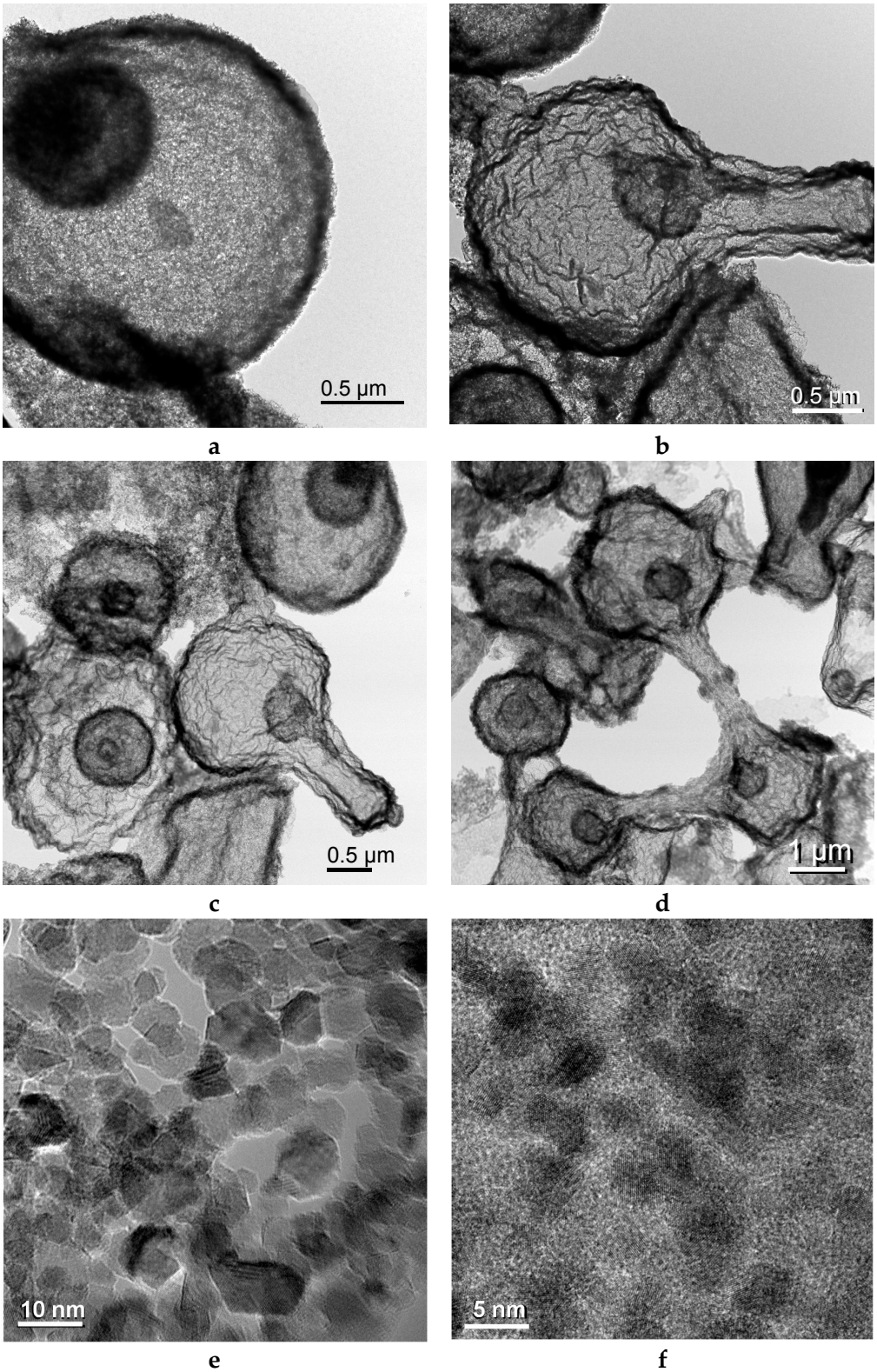

Figure 7. TEM-STEM pictures of hollow nickel oxide microspheres: (**a**–**d**) general views at rather similar magnifications; (**e**–**f**) high-resolution TEM pictures at higher magnifications.

Metal oxide nanoparticles have been already synthesised through the HTC technique based on starch [35,36] or glucose [2,51]. Titirici et al. [51] also obtained hollow crystalline iron oxide spheres with diameters of 1 µm, for which both the surface area and the thickness of the shell could be varied

depending on the experimental ratio carbohydrate/metal salt. For molar ratios from 5:1 up to 15:1, the surface area and the nanoparticles size increased from 22.0 to 83.5 $m^2 \cdot g^{-1}$ and from 16 to 22 nm, respectively. When saccharides were used as precursors, such hollow structures were assumed to form due to the strong complexation of metals at the more hydrophilic surface of the carbonaceous particles growing in the autoclave, whereas their inner part was more hydrophobic.

The surface area and the pore volumes of the present nano/micro-oxides are gathered in Table 1, and their values are related to their dispersion state: the higher is the surface area, the smaller is the particle size in the case of non-porous grains and/or the more dispersed is the material in the case of porous grains. However, whether the particles were porous or not, the whole oxides obtained this way were all porous materials simply due to their powdery character. Only the nickel oxide presented a high enough surface area allowing its investigation by adsorption of nitrogen, the other ones were evaluated by adsorption of krypton. As the latter isotherms are not very informative and are limited to a relative pressure of 0.2, only the nitrogen adsorption isotherm of nickel oxide is presented in Figure 8. The latter shows the typical features of a non-porous material (from the point of view of adsorption), in other words, it is characterised by a surface area which is only external, and the hysteresis loop observed at high relative pressure corresponds to capillary condensation in the mesoporous empty spaces between grains of nanometre size. As a result, only Ni oxide presents a non-negligible pore volume, see Table 1.

Table 1. Textural properties of nano/micro-oxides prepared by HTC of tannin-metal salts solutions followed by calcination in air.

Metal Salt	Specific Weight ($g \cdot cm^{-3}$) [a]	BET Surface Area ($m^2 \cdot g^{-1}$)	Pore Volume ($cm^3 \cdot g^{-1}$)	Particle Size (nm) [d]	Cystallite Size (nm) [e]
$VOSO_4 \cdot 5H_2O$	3.27	6.5 [c]	0.002 [c]	280	170
$(NH_4)_2Cr_2O_7$	4.27	20.7 [c]	0.006 [c]	70	55
$Ni(NH_4)_2(SO_4)_2 \cdot 6H_2O$	6.10	161 [b]	0.412 [b]	6	40
$(NH_4)_2Fe(SO_4)_2 \cdot 6H_2O$	5.24	29.2 [c]	0.008 [c]	40	9

[a] Measured by helium pycnometry; [b] Measured by adsorption of nitrogen; [c] Measured by adsorption of Kr at a relative pressure of 0.2; [d] Calculated from Equation (1); [e] Determined from Scherrer's equation applied to the data of Figure 9.

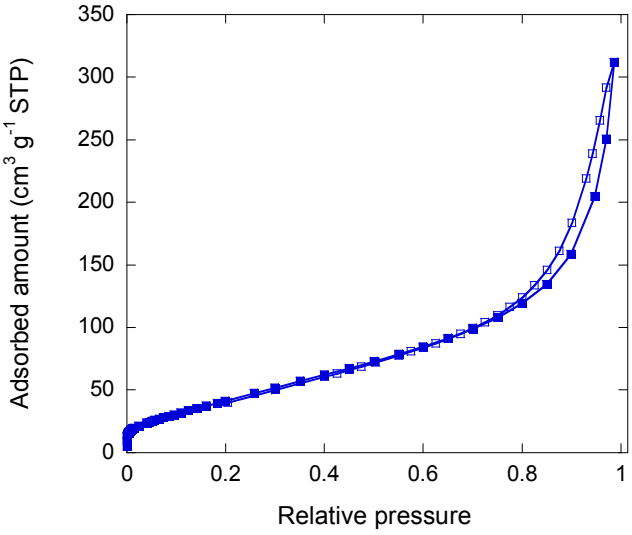

Figure 8. N_2 adsorption–desorption isotherm at −196 °C of the nickel nano-oxide. Full and open symbols correspond to adsorption and desorption, respectively.

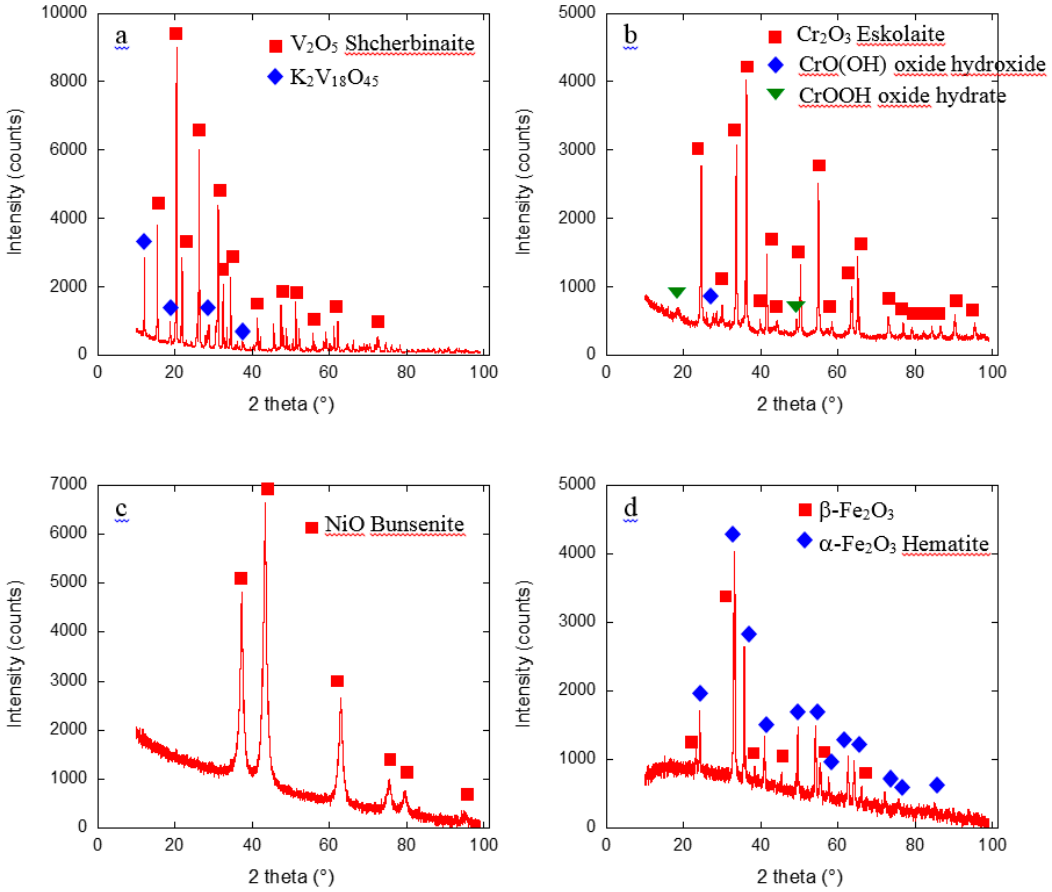

Figure 9. XRD patterns of nano/micro-oxides derived from calcination in air at 550 °C after HTC of tannin solutions containing: (**a**) V; (**b**) Cr; (**c**) Ni; and (**d**) Fe salts. The symbols above the main peaks correspond to the crystalline phases indicated on each plot.

The BET surface area measured on calcined nickel oxide, 161 $m^2 \cdot g^{-1}$, was much higher than the values reported by Titirici et al. [51], whereas those measured for the present iron, vanadium and chromium oxides were of the same order of magnitude: 29, 6.5 and 21 $m^2 \cdot g^{-1}$, respectively. Assuming that the grains are spherical (which is obviously not correct, especially for V oxide) and non-porous, the following equation roughly allows determining an equivalent diameter, d (µm), for a material having a specific weight ρ ($g \cdot cm^{-3}$) and an external surface area S ($m^2 \cdot g^{-1}$):

$$d = \frac{6}{\rho\, S} \quad (1)$$

About 280 and 70 nm were found for V and Cr oxides, respectively, using density values of 3.27 and 4.27 as measured by helium pycnometry, respectively (see Table 1). Those values of equivalent diameter were consistent with the particle sizes observed in the right parts of Figures 1 and 2, respectively. The same calculation can be done for hollow microspheres of Fe oxide, using a density of 5.24 and a measured surface area of 29 $m^2 \cdot g^{-1}$, leading to particle size of about 40 nm. The latter is in excellent agreement with what can be seen in Figure 6f. As for NiO hollow microspheres, of density and surface area of 6.10 and 161 $m^2 \cdot g^{-1}$, respectively, the calculated particle size was close to 6 nm. Again, such order of magnitude perfectly agrees with what can be seen in high-resolution TEM pictures of Figure 7e,f. Interestingly, hollow NiO microspheres having similar diameters were also produced by ultrasonic spray atomisation but their surface area was lower (11–30 $m^2 \cdot g^{-1}$, depending on the synthesis conditions) because made of bigger nanoparticles (average size 35–64 nm) [52].

The XRD spectra of nano/micro-oxides derived from HTC of V, Cr, Ni and Fe salts in the presence of tannins followed by calcination in air are presented in Figure 9. Based on them, the corresponding major crystalline phases were positively identified as shcherbinaite, eskolaite, bunsenite and hematite, respectively. A few other minor phases were also detected, such as $K_2V_{18}O_{45}$ (explained by the presence of potassium as a major inorganic impurity in tannin), hydrated chromium oxides, and β-Fe_2O_3. The presence of the main minerals is, however, in agreement with the densities determined by helium pycnometry, as the specific weight with can be calculated from the cell parameters and the cell unit atom content of each phase is 3.37, 5.23, 6.81 and 5.28 g·cm^{-3} for shcherbinaite, eskolaite, bunsenite, and hematite, respectively. Only the chromium oxide presented a significantly lower measured value of density (see again Table 1), attributed to the presence of hydrated phases. Finally, application of the well-known Scherrer's law to the data of Figure 9 allowed determining the crystallite sizes. Their values, associated with an uncertainty of ±2 nm, are given in Table 1 and can be compared with the particle sizes also presented in the same Table. The agreement between the two sets of values is very good, except for the biggest particles, but this finding is readily explained by the fact that XRD only accounts for crystallites, whose sizes are lower than—or equal to—those of particles.

2.2. Iron/Carbon Hybrid Materials

When pyrolysed at 900 °C in inert atmosphere instead of being calcined in air at 550 °C, the iron–carbon composite material obtained after HTC led to a mixture of iron and magnetite dispersed in graphitic carbon, as suggested by XRD results given in Figure 10.

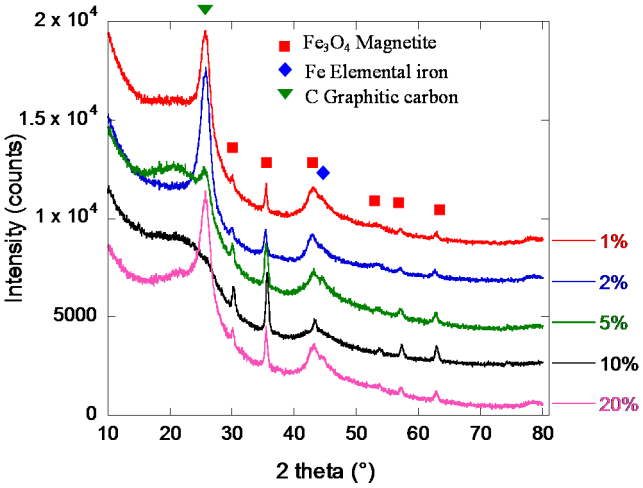

Figure 10. XRD patterns for carbon samples loaded with different percentages of iron, obtained by HTC of tannin-Fe(II) solutions, followed by pyrolysis at 900 °C under inert atmosphere. For clarity, the patterns were shifted in intensity with respect to each other.

Figure 11a,b show TEM pictures of such materials prepared with 2% and 20% of iron, respectively. The partial graphitisation can be clearly identified for both, and typical capsule-like structures made of oriented carbon layers can indeed be seen. Different mechanisms are reported in the literature to explain the graphitisation of carbon catalysed by transition metals such as iron, and leading to this particular kind of hollow carbon morphology. Thus, such capsules might correspond to the carbon formerly coating Fe nanoparticles and having been converted into a graphite-like material at their contact. Such a kind of graphitisation reaction indeed requires that the metal is directly in contact with carbon [53]. Moreover, the rest of the material is mainly based on a highly disordered carbon matrix, as already observed in other carbons pyrolysed in the presence of transition metals (see [53,54] and refs. therein). The size of graphitic capsules was about 10–20 nm, compatible with that of metal nanoparticles prepared in these conditions and that can indeed be observed in Figure 11 in the form of

dark spots. Moreover, the determination of the crystallite size by application of Scherrer's equation to the data of Figure 10 led to values of 20, 17, 14, 17 and 21 nm for materials containing 1%, 2%, 5%, 10% and 20% of iron. The uncertainty on those values of size, all in agreement with TEM observations, was ±2 nm. However, it is worth mentioning that Glatzel et al. [55] reported another mechanism based on the formation of liquid Fe–C eutectic nanodroplets during pyrolysis, which dissolve amorphous carbon and leave behind during their movement a trail of crystallized graphitic carbon shells. Such a mechanism cannot be completely discarded in the present case.

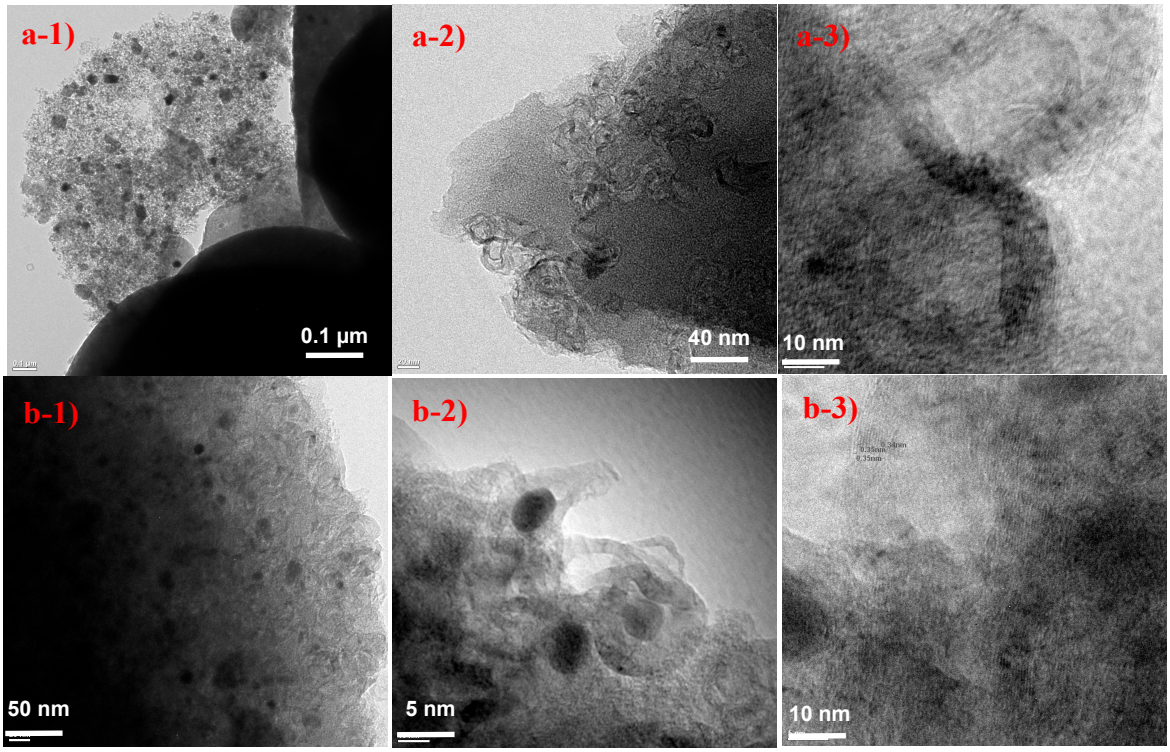

Figure 11. TEM pictures of (**a**) iron/carbon hybrid material loaded with 2% of Fe^{2+}, based on tannin-derived hydrothermal carbon prepared at 180 °C and pyrolysed at 900 °C, at different magnifications, showing iron nanoparticles and graphite-like capsules; (**b**) same as (**a**) but the material was loaded with 20% of iron.

The materials pyrolysed at 900 °C and containing 1%, 2%, 5%, 10% and 20% of iron presented skeletal densities of 2.25, 2.29, 2.32, 2.42 and 2.67, respectively. Such a trend is consistent with the increasing loading of the materials by iron, expected to produce an increasing level of graphitisation. This phenomenon was checked by Raman spectroscopy, and the corresponding spectra are shown in Figure 12. Although the spectra all looked similar and presented the typical morphology of highly disordered carbon, the relative intensities of the D and G bands located at 1350 ± 5 cm^{-1} and 1595 ± 5 cm^{-1}, respectively, clearly changed with the amount of Fe. As expected, more iron produced materials with more intense G bands, which directly correspond to more graphitised carbon. The ratio of the D to G band intensities is shown in the inset of Figure 12 and clearly shows such a trend. Such a characterisation method therefore seems much more accurate than XRD, for which calculated values of carbon "crystallite" size were all around 4–4.1 nm, whatever the sample. Likewise, no trend was observed when the interplanar distances d002 of the Fe-loaded carbons were calculated from the patterns of Figure 10, all having values within the very narrow range 0.337–0.338 (±0.002) nm. Raman spectroscopy therefore appears to be a much preferred and more sensitive investigation tool in the present case.

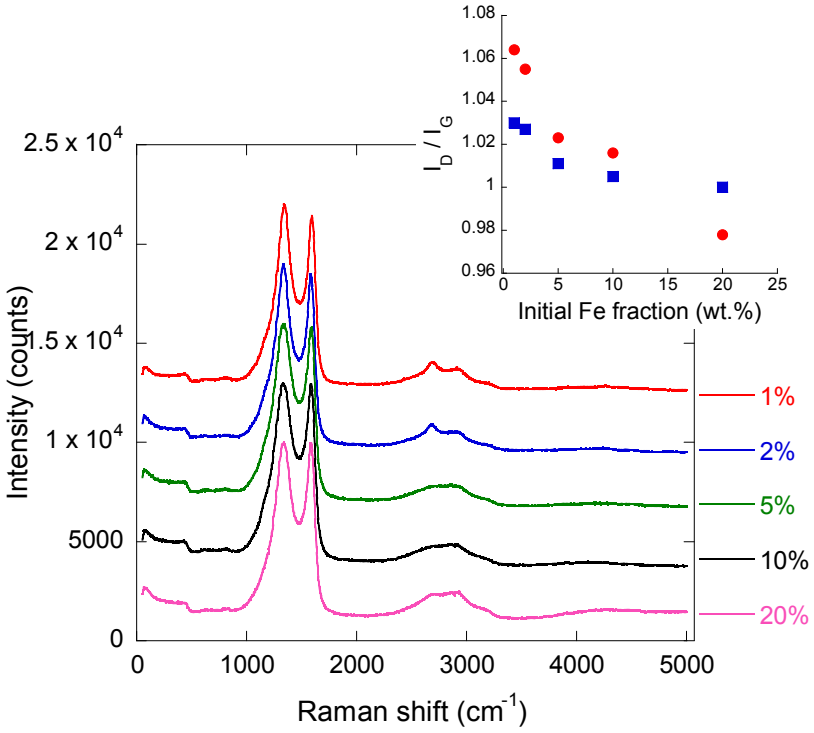

Figure 12. Raman spectra (shifted with respect to each other for clarity) of carbon materials loaded with increasing amounts of Fe (from top to bottom). The inset shows the corresponding changes of D to G band intensity ratio, either calculated after baseline correction and peak deconvolution (red discs) or directly determined from the raw spectra given here (blue squares).

Figure 13a,b show N_2 and CO_2 adsorption isotherms at −196 and 0°C, respectively, of most Fe–carbon hybrid materials. The one doped with 2% of iron presented curves and corresponding pore volumes that were almost identical to those of the material loaded at 1% Fe, so this sample was not shown for clarity. All N_2 isotherms were a combination of types I and IV, characteristic of micro-mesoporous solids according to the IUPAC classification [56]. The hysteresis loop indicates the existence of mesopores, whose volume V_m (See Table 2) was calculated as the difference between the total pore volume $V_{0.97}$ and the micropore volume calculated by application of the Non-Linear Density Functional Theory (NLDFT) model, $V_{\mu,NLDFT}$. Figure 13c shows the PSD calculated from both N_2 (Figure 13a) and CO_2 isotherms (Figure 13b). Two maxima were observed in the PSDs of all materials: one related to ultramicropores (<0.7 nm), and another one corresponding to mesopores (between 2 and 10 nm). The carbon materials presented higher ultramicropore volumes and lower mesopore volumes when increasing the iron content. Thus, the mesopore volume decreased from 25% to 12% with respect to the total pore volume ($V_{0.97}$).

Figure 13d shows the changes of BET surface areas and pore volumes by increasing the amount of iron. The BET surface area increased moderately with the iron content, and so did the surface area determined by the NLDFT method. S_{NLDFT} was found to be significantly higher than S_{BET} as the former indeed takes into account the narrow microporosity determined from CO_2 isotherms. The increasing surface area of the materials at increasing iron content might appear illogic as (i) Fe is heavier than C, and (ii) Fe is not expected to contribute to the surface area except through the external surface of its (nano)particles. However, increasing $(NH_4)_2Fe(SO_4)_2{\cdot}6H_2O$ addition produced a decrease of the hydrochar yield (i.e., the weight fraction of solid recovered after HTC of the tannin-metal salt solution) from 65% to 30% at 1 and 20 wt % of Fe, respectively, whereas the carbonisation yield (i.e., the weight fraction of solid recovered after pyrolysis of the hydrochar) was around 51%, irrespective to the hydrochar considered. The total yield to iron-loaded carbon materials based on the initial amount of

tannin (i.e., the HTC yield multiplied by the carbonisation yield), thus varied from 33% to 15%. The yield to carbon was much lower for the Fe-richest carbon materials. Although Ni catalysts have been more frequently used to increase the hydrothermal gasification of biomass [57], it is clear that Fe ions also have a catalytic effect on the production of gas, most probably leading to the activation of the carbon with a resultant higher surface area related to the corresponding production of narrow porosity.

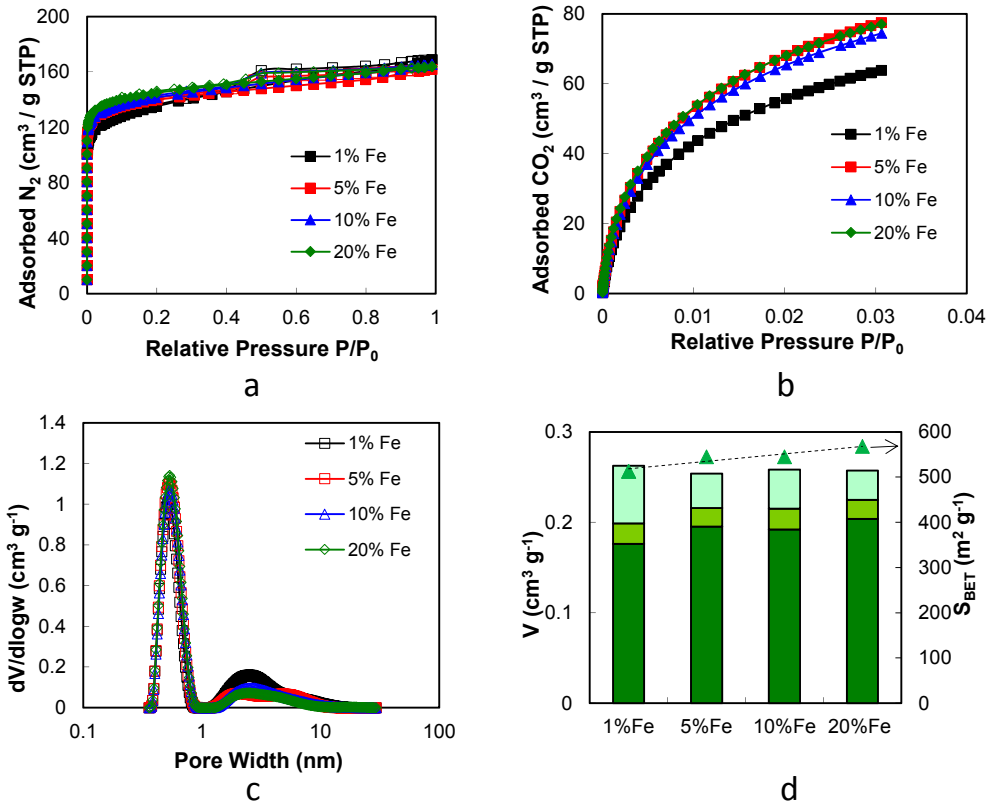

Figure 13. (**a**) Nitrogen adsorption–desorption isotherms (full and open symbols, respectively) at −196 °C for all samples after HTC and subsequent pyrolysis at 900 °C; (**b**) CO_2 adsorption isotherms at 0 °C for the same materials as in (**a**); (**c**) Pore size distributions determined by application of the NLDFT model to the data shown in (**a**) and (**b**); (**d**) Corresponding pore volumes classified according to their sizes: narrower than 0.7 nm (ultramicropores), between 0.7 and 2 nm (supermicropores); and between 2 and 50 nm (mesopores).

Table 2. Textural properties measured for porous carbons loaded with iron.

Fe–Carbon Hybrid Materials Containing:	S_{BET} ($m^2 \cdot g^{-1}$)	S_{DFT} ($m^2 \cdot g^{-1}$)	$V_{0.97}$ ($cm^3 \cdot g^{-1}$)	$V_{\mu,N2}$ ($cm^3 \cdot g^{-1}$)	$V_{\mu,CO2}$ ($cm^3 \cdot g^{-1}$)	$V_{\mu,NLDFT}$ ($cm^3 \cdot g^{-1}$)	V_m ($cm^3 \cdot g^{-1}$)	ρ ($cm^3 \cdot g^{-1}$)
1% Fe	513	756	0.26	0.19	0.21	0.20	0.06	2.25
5% Fe	545	808	0.26	0.21	0.26	0.22	0.04	2.32
10% Fe	545	805	0.26	0.21	0.25	0.22	0.04	2.42
20% Fe	568	841	0.25	0.21	0.25	0.22	0.03	2.67

The catalytic effect of Fe on tar yield reduction during dry biomass gasification is indeed well-known [58], and Fe is usually added to Ni catalysts to increase the selectivity to hydrogen production [59]. Therefore, the higher evolution of gases, essentially H_2 and CO_2, during the hydrothermal process [60] is expected to favour the higher porosity and surface area after carbonisation of the iron-loaded carbon materials. $V_{\mu,N2}$ was always lower than the one determined by DR method applied to the CO_2 isotherm, $V_{\mu,CO2}$, meaning that the materials had an important fraction of narrow

microporosity that was not accessible to N_2 at −196 °C, due to the low N_2 diffusion kinetics at this very low temperature. Table 2 also presents the micropore volumes calculated by the application of the NLDFT model to both N_2 and CO_2 isotherms considered simultaneously. Differences between the micropore volumes determined by DR and NLDFT models are attributed to the overestimation of the micropore volume when applying the DR method.

All the materials listed in Table 2 were ferromagnetic, as expected from their iron content and as it can be easily observed by approaching a rare-earth magnet to the glass vials containing them. Magnetic porous carbons have been already prepared and suggested for a number of adsorption applications in the liquid phase [61–63]. Iron-containing activated carbons can indeed be more easily recovered out of the effluents after some targeted pollutants are removed. The present materials probably have surface areas and porous volumes that still are too low for this kind of application, but they should become perfectly suitable after a short physical activation step. The corresponding gasification of the carbon is indeed known to be catalysed by metals, and therefore the surface area and the pore volumes are expected to develop quickly. As a consequence, the adsorption capacity will be improved and the iron content will increase further, making those materials even more magnetic per unit weight. The method presented here is then quite simple and cost-effective for preparing iron-loaded porous carbons from virtually any precursor soluble in water.

3. Experimental section

3.1. Materials

3.1.1. Tannin

Mimosa tannin was kindly supplied by the company SilvaChimica (St Michele Mondovi, Italy). The general procedure for extracting them consists in leaching wattle (*Acacia mearnsii*) barks using 1% sodium bisulphite in water at 70 °C. The resultant solution is then concentrated and spray-dried, leading to a light-brown powder which generally contains 80%–82% of actual phenolic flavonoid materials, 4%–6% of water, 1% of amino and imino acids, the remainder being monomeric and oligomeric carbohydrates, in general broken pieces of hemicelluloses.

3.1.2. Synthesis of Metal Nano/Micro Oxides and Iron/Carbon Hybrid Materials

Different metal salts (purity > 97%) were dissolved and treated in hydrothermal conditions in the presence of Mimosa tannin for the production of crystalline metal oxides:

- One vanadium salt: vanadyl sulphate pentahydrate $VOSO_4 \cdot 5H_2O$, supplied by VWR (Radnor, PA, USA);
- One chromium salt: ammonium chromate $(NH_4)_2Cr_2O_7$, supplied by Sigma-Aldrich (Saint-Louis, MO, USA);
- One nickel salt: ammonium nickel sulphate hexahydrate $Ni(NH_4)_2(SO_4)_2 \cdot 6H_2O$, supplied by Sigma-Aldrich;
- One iron salt: ammonium iron(II) sulphate hexahydrate $(NH_4)_2Fe(SO_4)_2 \cdot 6H_2O$, supplied by Merck (Darmstadt, Germany).

Knowing that the average molecular mass of Mimosa tannin is approximately 1000 $g \cdot mol^{-1}$, we followed the method applied by Titirici et al. [51] to the HTC of glucose with metal salts by using a molar ratio tannin/metal salt of 5:1. In a typical synthesis, samples were prepared by mixing 20 mL of water in which 3.75 g of tannin was dissolved with 10 mL of water in which each metal salt was dissolved. Both solutions were mixed immediately during 10 min and then the final black solution was placed in an autoclave and then in an oven at 180 °C for 24 h. The inner volume of the autoclave was 100 cm^3, so that the volume of liquid placed inside, around 33 cm^3, was one-third of its capacity. The final black powder was filtered and washed with water before being dried overnight in a vacuum oven

at 80 °C. Calcination was carried out in a ceramic muffle furnace heated at 4 °C·min^{-1} up to 550 °C (4 h dwell time), allowing burning all organic matters and hence recovering porous metal oxides.

In the case of ammonium iron(II) sulphate hexahydrate $(NH_4)_2Fe(SO_4)_2 \cdot 6H_2O$, materials containing various fractions of iron were also prepared and were investigated after pyrolysis in nitrogen at 900 °C. The amount of iron salt was calculated as follows, depending on the desired final percentage of iron which was within the range 1–20 wt % with respect to carbon after pyrolysis. According to elemental analysis, the carbon content in Mimosa tannin is 53.8 wt % [50]. Therefore, in 3.75 g of tannin used in all experiments, 2 g is pure C. Different amounts of Fe^{2+} ions: 1%, 2%, 5%, 10% and 20% with respect to C present in tannin (2 g) were then used, hence the amount of metal salt varied from 0.14 to 2.82 g for getting 1 to 20 wt % of Fe in the final materials. The HTC treatments were performed as already explained for the other metal salts. The solid recovered after HTC, washing and drying, was then submitted to pyrolysis under nitrogen flow in a tubular furnace at a heating rate of 1 °C·min^{-1} up to 900 °C (1 h dwell time).

3.2. Materials Characterisation

3.2.1. SEM and TEM Observations

Transmission electron microscopy (TEM) studies were carried out using a CM200 apparatus (FEI/Philips, Hillsboro, OR, USA) and, in a few cases, using a JEM–ARM 200F Cold FEG TEM/STEM (JEOL, Tokyo, Japan) operating at 200 kV and equipped with a spherical aberration probe corrector. For that purpose, the materials were ground in an agate mortar if required (i.e., only for Fe/carbon hybrid materials, not for pure metal oxides), and then dispersed in chloroform by sonication. A drop of the dispersion was laid down on a TEM grid and dried before observation. Scanning electron microscopy (SEM) studies were carried out with using a Quanta 600 FEG equipped with a detector of secondary electrons (FEI, Hillsboro, OR, USA).

3.2.2. Pore Texture Analysis

Pore texture parameters were obtained by nitrogen or krypton adsorption at −196 °C using a ASAP 2020 automatic apparatus (Micromeritics, Norcross, GA, USA). N_2 adsorption allowed determining porous volumes of samples exhibiting high-enough surface areas, whereas those presenting much lower values were better investigated through adsorption of krypton. For that purpose, all samples were degassed for 48 h under vacuum at 250 °C prior to any adsorption experiment. N_2 and CO_2 adsorption was also carried out in the case of carbon materials loaded with various amounts of iron. The corresponding isotherms were treated for obtaining (i) apparent surface area: S_{BET}, from the BET calculation method applied to a range of relative pressures such that the BET constant was always positive [64]; (ii) micropore volume: V_μ, from the Dubinin–Radushkevich (DR) method, microporous surface area: S_μ, and external surface area: S_{ext}, from the *t*-plot method, based on the representation of the isotherm versus the thickness of the adsorbed layer on a non-porous reference (carbon) material [65]; (iii) total pore volume: $V_{0.97}$, defined as the volume of liquid nitrogen corresponding to the amount adsorbed at a relative pressure $P/P_0 = 0.97$ [66]; (iv) mesopore volume: V_m, calculated as the difference $V_{0.97} - V_\mu$; (v) pore-size distribution (PSD), calculated by application of the Non-Linear Density Functional Theory (NLDFT) model to N_2 and CO_2 isotherms [67]. The SAIEUS software, provided by Micromeritics, allowed obtaining one single PSD from the two, N_2 and CO_2, isotherms. Finally, the skeletal density of all materials was measured using an AccuPyc II 1340 pycnometer (Micromeritics, Norcross, GA, USA), using 99.99% purity helium.

3.2.3. X-Ray Diffraction

X-ray diffraction (XRD) patterns were recorded with an X'Pert Pro diffractometer (PANalytical, Eindhoven, The Netherlands). The latter was used in a Bragg–Brentano configuration in reflection mode and was equipped with a Cu (Kα radiation) anticathode and a high-speed multichannel

X'Celerator detector in scanning mode with an active length (2θ) = 2.122° (scanning range 2θ = 10°–80°; step size = 0.03342°; time per step size = 104.78 s, and number of points = 2096).

3.2.4. Raman Spectroscopy

Raman spectroscopy was only applied to iron/carbon hybrid materials obtained after pyrolysis at 900 °C of materials prepared by HTC of tannin–iron salt mixtures. The aim was to observe the possible catalytic graphitisation of tannin-derived carbon, which was never reported so far. Raman spectra were obtained with a Horiba XploRa Raman spectrometer without sample preparation. The spectra were collected under a microscope using a 100× objective. The Raman-scattered light was dispersed by a holographic grating with 1200 lines per mm and detected by a charge coupled device (CCD) camera. A laser of wavelength 532 nm, filtered at 10% of its nominal power was used. The corresponding incident power, around 1.8 mW, was low enough to avoid any heating or damage of the samples. Each spectrum was obtained by accumulation of two spectra recorded from 50 to 5000 cm^{-1} over 120 s, and was fitted by using four mixed Gaussian–Lorentzian profiles for the bands D4, D1, D3, G and D2 appearing at increasingly high wavenumbers (see for example [68]).

4. Conclusions

Mimosa tannin was used as a cheap, renewable and valuable organic precursor for preparing two very different kinds of inorganic porous materials through a hydrothermal route. For that purpose, four different V, Cr, Ni and Fe salts were dissolved in the tannin aqueous solution and submitted to hydrothermal carbonisation at 180 °C for 24 h. The resultant solid was recovered and subsequently either calcined at 550 °C in air—thus leading to porous oxides, or pyrolysed at 900 °C in nitrogen—thus leading to porous metal/carbon hybrid materials.

Calcination in air produced porous oxides having two distinct morphologies: nanoparticles on the one hand with V and Cr, and hollow microspheres on the other hand with Ni and Fe. These different findings were assumed to originate from different complexation behaviours of metal ions by tannins. All oxides were crystallised and could be positively identified based on their XRD patterns. They all presented a purely external surface area, based on which calculating the equivalent size of the constitutive oxide nanoparticles was possible.

Pyrolysis in inert atmosphere was carried out with hydrochars loaded with various amounts of iron. The reaction of carbon with iron oxide at 900 °C produced porous carbon materials containing mainly magnetite, although elemental iron was also evidenced. Iron induced the partial graphitisation of carbon, as proved by Raman and TEM studies, as well as an increase of pore volume and surface area. The latter finding was explained by the ability of Fe to catalyse carbon gasification. An additional activation step might easily improve the textural properties further for converting these materials into magnetic activated carbons for depollution purposes.

Acknowledgments: The IJL research team gratefully acknowledges the financial support of the CPER 2007–2013 "Structuration du Pôle de Compétitivité Fibres Grand'Est" (Competitiveness Fibre Cluster), through local (Conseil Général des Vosges), regional (Région Lorraine), national (DRRT and FNADT) and European (FEDER) funds. Part of this work was supported by CHEERS project (FEDER funds).

Author Contributions: Vanessa Fierro, Julien Parmentier and Alain Celzard conceived and designed the experiments; Flavia L. Braghiroli and Philippe Gadonneix performed the syntheses; Vanessa Fierro and Alain Celzard performed adsorption and Raman experiments, respectively, and all related analyses; Andrzej Szczurek, Jaafar Ghanbaja and Ghouti Medjahdi carried out SEM, TEM and XRD studies, respectively; Vanessa Fierro and Alain Celzard analysed the other data; Flavia L. Braghiroli, Vanessa Fierro and Alain Celzard wrote the paper.

Conflicts of Interest: The authors declare no conflict of interest.

References

1. Terris, B.D.; Thomson, T. Nanofabricated and self-assembled magnetic structures as data storage media. *J. Phys. Appl. Phys.* **2005**, *38*, R199. [CrossRef]

2. Sun, S.; Murray, C.B.; Weller, D.; Folks, L.; Moser, A. Monodisperse FePt nanoparticles and ferromagnetic FePt nanocrystal superlattices. *Science* **2000**, *287*, 1989–1992. [CrossRef] [PubMed]
3. Wang, Y.; Wei, W.; Maspoch, D.; Wu, J.; Dravid, V.P.; Mirkin, C.A. Superparamagnetic Sub-5 nm Fe@C Nanoparticles: Isolation, Structure, Magnetic Properties, and Directed Assembly. *Nano Lett.* **2008**, *8*, 3761–3765. [CrossRef] [PubMed]
4. Li, G.; Joshi, V.; White, R.L.; Wang, S.X.; Kemp, J.T.; Webb, C.; Davis, R.W.; Sun, S. Detection of single micron-sized magnetic bead and magnetic nanoparticles using spin valve sensors for biological applications. *J. Appl. Phys.* **2003**, *93*, 7557–7559. [CrossRef]
5. Ren, X.; Meng, X.; Chen, D.; Tang, F.; Jiao, J. Using silver nanoparticle to enhance current response of biosensor. *Biosens Bioelectron.* **2005**, *21*, 433–437. [CrossRef] [PubMed]
6. Moreno-Mañas, M.; Pleixats, R. Formation of Carbon–Carbon Bonds under Catalysis by Transition-Metal Nanoparticles. *Acc. Chem. Res.* **2003**, *36*, 638–643. [CrossRef] [PubMed]
7. Wang, C.-B.; Zhang, W. Synthesizing Nanoscale Iron Particles for Rapid and Complete Dechlorination of TCE and PCBs. *Environ. Sci. Technol.* **1997**, *31*, 2154–2156. [CrossRef]
8. Lin, Y.-T.; Weng, C.-H.; Chen, F.-Y. Effective removal of AB24 dye by nano/micro-size zero-valent iron. *Sep. Purif. Technol.* **2008**, *64*, 26–30. [CrossRef]
9. Ban, Z.; Barnakov, Y.A.; Li, F.; Golub, V.O.; O'Connor, C.J. The synthesis of core–shell iron@gold nanoparticles and their characterization. *J. Mater. Chem.* **2005**, *15*, 4660–4662. [CrossRef]
10. Gupta, A.K.; Gupta, M. Synthesis and surface engineering of iron oxide nanoparticles for biomedical applications. *Biomaterials* **2005**, *26*, 3995–4021. [CrossRef] [PubMed]
11. Lee, J.-H.; Huh, Y.-M.; Jun, Y.; Seo, J.; Jang, J.; Song, H.-T.; Kim, S.; Cho, E.-J.; Yoon, H.-G.; Suh, J.-S.; et al. Artificially engineered magnetic nanoparticles for ultra-sensitive molecular imaging. *Nat. Med.* **2007**, *13*, 95–99. [CrossRef] [PubMed]
12. Tang, N.J.; Chen, W.; Zhong, W.; Jiang, H.Y.; Huang, S.L.; Du, Y.W. Highly stable carbon-coated Fe/SiO_2 composites: Synthesis, structure and magnetic properties. *Carbon* **2006**, *44*, 423–427. [CrossRef]
13. Ma, C.; Luo, B.; Song, H.; Zhi, L. Preparation of carbon-encapsulated metal magnetic nanoparticles by an instant pyrolysis method. *New Carbon Mater.* **2010**, *25*, 199–204. [CrossRef]
14. Zhang, D.; Wei, S.; Kaila, C.; Su, X.; Wu, J.; Karki, A.B.; Young, D.P.; Guo, Z. Carbon-stabilized iron nanoparticles for environmental remediation. *Nanoscale* **2010**, *2*, 917–919. [CrossRef] [PubMed]
15. Fung, K.K.; Qin, B.; Zhang, X.X. Passivation of α-Fe nanoparticle by epitaxial γ-Fe_2O_3 shell. *Mater. Sci. Eng. A* **2000**, *286*, 135–138. [CrossRef]
16. Zhang, X.F.; Dong, X.L.; Huang, H.; Lv, B.; Zhu, X.G.; Lei, J.P.; Ma, S.; Liu, W.; Zhang, Z.D. Synthesis, growth mechanism and magnetic properties of SiO_2-coated Co nanocapsules. *Acta Materialia* **2007**, *55*, 3727–3733. [CrossRef]
17. Tokoro, H.; Nakabayashi, T.; Fujii, S.; Zhao, H.; Häfeli, U.O. Magnetic iron particles with high magnetization useful for immunoassay. *J. Mag. Mag. Mater.* **2009**, *321*, 1676–1678. [CrossRef]
18. Wilson, J.L.; Poddar, P.; Frey, N.A.; Srikanth, H.; Mohomed, K.; Harmon, J.P.; Kotha, S.; Wachsmuth, J. Synthesis and magnetic properties of polymer nanocomposites with embedded iron nanoparticles. *J. Appl. Phys.* **2004**, *95*, 1439–1443. [CrossRef]
19. Zhu, L.; Ma, J.; Jia, N.; Zhao, Y.; Shen, H. Chitosan-coated magnetic nanoparticles as carriers of 5-fluorouracil: Preparation, characterization and cytotoxicity studies. *Colloids Surf. B Biointerfaces* **2009**, *68*, 1–6. [CrossRef] [PubMed]
20. Leslie-Pelecky, D.L.; Rieke, R.D. Magnetic Properties of Nanostructured Materials. *Chem. Mater.* **1996**, *8*, 1770–1783. [CrossRef]
21. Xu, Z.P.; Zeng, Q.H.; Lu, G.Q.; Yu, A.B. Inorganic nanoparticles as carriers for efficient cellular delivery. *Chem. Eng. Sci.* **2006**, *61*, 1027–1040. [CrossRef]
22. Fernández-García, M.; Martínez-Arias, A.; Hanson, J.C.; Rodriguez, J.A. Nanostructured Oxides in Chemistry: Characterization and Properties. *Chem. Rev.* **2004**, *104*, 4063–4104. [CrossRef] [PubMed]
23. Wu, J.H.; Ko, S.P.; Liu, H.L.; Jung, M.H.; Lee, J.H.; Ju, J.S.; Kim, Y.K. Sub 5 nm Fe_3O_4 nanocrystals via coprecipitation method. *Colloids Surf. Physicochem. Eng. Asp.* **2008**, *313–314*, 268–272. [CrossRef]
24. Meng, H.; Zhang, Z.; Zhao, F.; Qiu, T.; Yang, J. Orthogonal optimization design for preparation of Fe_3O_4 nanoparticles via chemical coprecipitation. *Appl. Surf. Sci.* **2013**, *280*, 679–685. [CrossRef]

25. Zhang, X.; Jiang, W.; Gong, X.; Zhang, Z. Sonochemical synthesis and characterization of magnetic separable Fe_3O_4/Ag composites and its catalytic properties. *J. Alloys Comp.* **2010**, *508*, 400–405. [CrossRef]
26. Feng, J.; Mao, J.; Wen, X.; Tu, M. Ultrasonic-assisted in situ synthesis and characterization of superparamagnetic Fe_3O_4 nanoparticles. *J. Alloys Comp.* **2011**, *509*, 9093–9097. [CrossRef]
27. Lemine, O.M.; Omri, K.; Zhang, B.; Mir, L.E.; Sajieddine, M.; Alyamani, A.; Bououdina, M. Sol–gel synthesis of 8 nm magnetite (Fe_3O_4) nanoparticles and their magnetic properties. *Superlattices Microstruct.* **2012**, *52*, 793–799. [CrossRef]
28. Cui, H.; Liu, Y.; Ren, W. Structure switch between α-Fe_2O_3, γ-Fe_2O_3 and Fe_3O_4 during the large scale and low temperature sol–gel synthesis of nearly monodispersed iron oxide nanoparticles. *Adv. Powder Technol.* **2013**, *24*, 93–97. [CrossRef]
29. Peng, D.; Beysen, S.; Li, Q.; Jian, J.; Sun, Y.; Jiwuer, J. Hydrothermal growth of octahedral Fe_3O_4 crystals. *Particuology* **2009**, *7*, 35–38. [CrossRef]
30. Cheng, Z.; Chu, X.; Yin, J.; Zhong, H.; Xu, J. Surfactantless synthesis of Fe_3O_4 magnetic nanobelts by a simple hydrothermal process. *Mater. Lett.* **2012**, *75*, 172–174. [CrossRef]
31. Gao, G.; Qiu, P.; Qian, Q.; Zhou, N.; Wang, K.; Song, H.; Fu, H.; Cui, D. PEG-200-assisted hydrothermal method for the controlled-synthesis of highly dispersed hollow Fe_3O_4 nanoparticles. *J. Alloys Comp.* **2013**, *574*, 340–344. [CrossRef]
32. Daou, T.J.; Pourroy, G.; Bégin-Colin, S.; Grenèche, J.M.; Ulhaq-Bouillet, C.; Legaré, P.; Bernhardt, P.; Leuvrey, C.; Rogez, G. Hydrothermal Synthesis of Monodisperse Magnetite Nanoparticles. *Chem. Mater.* **2006**, *18*, 4399–4404. [CrossRef]
33. Hayashi, H.; Hakuta, Y. Hydrothermal Synthesis of Metal Oxide Nanoparticles in Supercritical Water. *Materials* **2010**, *3*, 3794–3817. [CrossRef]
34. Mitchell, E.; De Souza, F.; Gupta, R.K.; Kahol, P.K.; Kumar, D.; Dong, L.; Gupta, B.K. Probing on the hydrothermally synthesized iron oxide nanoparticles for ultra-capacitor applications. *Powder Technol.* **2015**, *272*, 295–299. [CrossRef]
35. Yu, S.H.; Cui, X.J.; Li, L.L.; Li, K.; Yu, B.; Antonietti, M.; Cölfen, H. From Starch to Metal/Carbon Hybrid Nanostructures: Hydrothermal Metal-Catalyzed Carbonization. *Adv. Mater.* **2004**, *16*, 1636–1640. [CrossRef]
36. Cui, X.; Antonietti, M.; Yu, S.-H. Structural Effects of Iron Oxide Nanoparticles and Iron Ions on the Hydrothermal Carbonization of Starch and Rice Carbohydrates. *Small* **2006**, *2*, 756–759. [CrossRef] [PubMed]
37. Luo, L.-B.; Yu, S.-H.; Qian, H.-S.; Gong, J.-Y. Large scale synthesis of uniform silver@carbon rich composite (carbon and cross-linked PVA) sub-microcables by a facile green chemistry carbonization approach. *Chem. Commun.* **2006**, 793–795. [CrossRef] [PubMed]
38. Titirici, M.-M. (Ed.) *Sustainable Carbon Materials from Hydrothermal Processes*; Wiley: Chichester, West Sussex, UK, 2013.
39. Braghiroli, F.L.; Fierro, V.; Parmentier, J.; Vidal, L.; Gadonneix, P.; Celzard, A. Hydrothermal carbons produced from tannin by modification of the reaction medium: Addition of H^+ and Ag^+. *Ind. Crops Prod.* **2015**, *77*, 364–374. [CrossRef]
40. Braghiroli, F.L.; Fierro, V.; Izquierdo, M.T.; Parmentier, J.; Pizzi, A.; Celzard, A. Nitrogen-doped carbon materials produced from hydrothermally treated tannin. *Carbon* **2012**, *50*, 5411–5420. [CrossRef]
41. Braghiroli, F.L.; Fierro, V.; Szczurek, A.; Stein, N.; Parmentier, J.; Celzard, A. Electrochemical performances of hydrothermal tannin-based carbons doped with nitrogen. *Ind. Crops Prod.* **2015**, *70*, 332–340. [CrossRef]
42. Braghiroli, F.L.; Fierro, V.; Szczurek, A.; Stein, N.; Parmentier, J.; Celzard, A. Hydrothermally treated aminated tannin as precursor of N-doped carbon gels for supercapacitors. *Carbon* **2015**, *90*, 63–74. [CrossRef]
43. Hagerman, A.E.; Riedl, K.M.; Jones, G.A.; Sovik, K.N.; Ritchard, N.T.; Hartzfeld, P.W.; Riechel, T.L. High Molecular Weight Plant Polyphenolics (Tannins) as Biological Antioxidants. *J. Agric. Food Chem.* **1998**, *46*, 1887–1892. [CrossRef]
44. Yokozawa, T.; Chen, C.P.; Dong, E.; Tanaka, T.; Nonaka, G.I.; Nishioka, I. Study on the inhibitory effect of tannins and flavonoids against the 1,1-diphenyl-2 picrylhydrazyl radical. *Biochem. Pharmacol.* **1998**, *56*, 213–222. [CrossRef]
45. Amarowicz, R.; Troszyńska, A.; Shahidi, F. Antioxidant Activity of Almond Seed Extract and Its Fractions. *J. Food Lipids* **2005**, *12*, 344–358. [CrossRef]
46. Saint-Cricq de Gaulejac, N.; Provost, C.; Vivas, N. Comparative Study of Polyphenol Scavenging Activities Assessed by Different Methods. *J. Agric. Food Chem.* **1999**, *47*, 425–431. [CrossRef] [PubMed]

47. Karamać, M. In-vitro study on the efficacy of tannin fractions of edible nuts as antioxidants. *Eur. J. Lipid Sci. Technol.* **2009**, *111*, 1063–1071. [CrossRef]
48. Szczurek, A.; Fierro, V.; Pizzi, A.; Stauber, M.; Celzard, A. A new method for preparing tannin-based foams. *Ind. Crops Prod.* **2014**, *54*, 40–53. [CrossRef]
49. Szczurek, A.; Martinez de Yuso, A.; Fierro, V.; Pizzi, A.; Celzard, A. Tannin-based monoliths from emulsion-templating. *Mater. Design* **2015**, *79*, 115–126. [CrossRef]
50. Braghiroli, F.L.; Fierro, V.; Izquierdo, M.T.; Parmentier, J.; Pizzi, A.; Celzard, A. Kinetics of the hydrothermal treatment of tannin for producing carbonaceous microspheres. *Bioresour. Technol.* **2014**, *151*, 271–277. [CrossRef] [PubMed]
51. Titirici, M.-M.; Antonietti, M.; Thomas, A. A Generalized Synthesis of Metal Oxide Hollow Spheres Using a Hydrothermal Approach. *Chem. Mater.* **2006**, *18*, 3808–3812. [CrossRef]
52. Yudin, A.; Shatrova, N.; Khaydarov, B.; Kuznetsov, D.; Dzidziguri, E.; Issi, J.-P. Synthesis of hollow nanostructured nickel oxide microspheres by ultrasonic spray atomization. *J. Aerosol Sci.* **2016**, *98*, 30–40. [CrossRef]
53. Sevilla, M.; Fuertes, A.B. Catalytic graphitization of templated mesoporous carbons. *Carbon* **2006**, *44*, 468–474. [CrossRef]
54. Jana, P.; Palomo del Barrio, E.; Fierro, V.; Medjahdi, G.; Celzard, A. Design of carbon foams for seasonal solar thermal energy storage. *Carbon* **2016**, *109*, 771–787. [CrossRef]
55. Glatzel, S.; Schnepp, Z.; Giordano, C. From Paper to Structured Carbon Electrodes by Inkjet Printing. *Angew. Chem. Int. Ed.* **2013**, *52*, 2355–2358. [CrossRef] [PubMed]
56. Sing, K.S.W. Reporting physisorption data for gas/solid systems with special reference to the determination of surface area and porosity (Recommendations 1984). *Pure Appl. Chem.* **1985**, *57*, 603–619. [CrossRef]
57. Elliott, D.C. Catalytic hydrothermal gasification of biomass. *Biofuels Bioprod. Biorefining* **2008**, *2*, 254–265. [CrossRef]
58. Devi, L.; Craje, M.; Thüne, P.; Ptasinski, K.J.; Janssen, F.J.J.G. Olivine as tar removal catalyst for biomass gasifiers: Catalyst characterization. *Appl. Catal. Gen.* **2005**, *294*, 68–79. [CrossRef]
59. Courson, C.; Petit, C.; Kiennemann, A.; Foscolo, P.U.; Rapagnà, S.; Matera, M. Catalyseur pour la gazèification de la biomasse en lit fluidisé, procédé d'obtention et utilisations d'un tel catalyseur. European Patent PCT/FR01/01547, 18 May 2001.
60. Kruse, A.; Funke, A.; Titirici, M.-M. Hydrothermal conversion of biomass to fuels and energetic materials. *Curr. Opin. Chem. Biol.* **2013**, *17*, 515–521. [CrossRef] [PubMed]
61. Oliveira, L.C. A.; Rios, R.V. R.A.; Fabris, J.D.; Garg, V.; Sapag, K.; Lago, R.M. Activated carbon/iron oxide magnetic composites for the adsorption of contaminants in water. *Carbon* **2002**, *40*, 2177–2183. [CrossRef]
62. Yang, N.; Zhu, S.; Zhang, D.; Xu, S. Synthesis and properties of magnetic Fe_3O_4-activated carbon nanocomposite particles for dye removal. *Mater. Lett.* **2008**, *62*, 645–647. [CrossRef]
63. Zhou, L.; Shao, Y.; Liu, J.; Ye, Z.; Zhang, H.; Ma, J.; Jia, Y.; Gao, W.; Li, Y. Preparation and Characterization of Magnetic Porous Carbon Microspheres for Removal of Methylene Blue by a Heterogeneous Fenton Reaction. *ACS Appl. Mater. Interfaces* **2014**, *6*, 7275–7285. [CrossRef] [PubMed]
64. Brunauer, S.; Emmett, P.H.; Teller, E. Adsorption of Gases in Multimolecular Layers. *J. Am. Chem. Soc.* **1938**, *60*, 309–319. [CrossRef]
65. Lippens, B. Studies on pore systems in catalysts V. The t method. *J. Catal.* **1965**, *4*, 319–323. [CrossRef]
66. Gregg, S.J.; Sing, K.S.W. *Adsorption, Surface Area, and Porosity*; Academic Press: London, UK, 1991.
67. Tarazona, P. Solid-fluid transition and interfaces with density functional approaches. *Proc. 14th Eur. Conf. Surf. Sci.* **1995**, *331*, 989–994. [CrossRef]
68. Pawlyta, M.; Rouzaud, J.-N.; Duber, S. Raman microspectroscopy characterization of carbon blacks: Spectral analysis and structural information. *Carbon* **2015**, *84*, 479–490. [CrossRef]